Nuclear Engineering and Technology 54 (2022) 117–129

Contents lists available at ScienceDirect

Nuclear Engineering and Technology

journal homepage: www.elsevier.com/locate/net

Original article

Study on blockage after downward discharge of the molten metallic fuel with radiographic visualization

Min Ho Lee [a], Dong Wook Jerng [b, **], In Cheol Bang [a, *]

[a] Department of Nuclear Engineering Ulsan National Institute of Science and Technology (UNIST) 50 UNIST-gil, Ulju-gun, Ulsan, 44919, Republic of Korea
[b] School of Energy Systems Engineering Chung Ang Univ. Rep. of Korea 84 Heukseok-ro, Dongjak-gu, Seoul, 06974, Republic of Korea

ARTICLE INFO

Article history:
Received 3 February 2021
Received in revised form
28 May 2021
Accepted 10 July 2021
Available online 15 July 2021

Keywords:
SFR
Hypothetical core disruptive accident (HCDA)
Lower discharge
Lower structure
Pressure drop
Coolability

ABSTRACT

The downward discharge of the molten fuel to the lower structure of the fuel assembly could increase of the pressure drop and degrade of coolability of the assembly. To analyze the phenomena, experiments for the generation of the debris bed were conducted as LOF-DT series. Based on the debris bed in the LOF-DT, pressure drop experiment was conducted with intact and blocked component. Parametric study on the pressure drop was conducted by CFD. The LOF-DT experiments were conducted for the position and porosity of the debris bed. 85% of the debris were sedimented in the lower reflector, and 15% were in the nose piece, approximately. Porosity of the debris bed were about 0.7 and 0.85 in the lower reflector and nose piece, respectively. Pressure drop increased significantly with debris bed, especially in the lower reflector. More than 120 time of the pressure drop increased in the lower reflector, while only 10% increased in the nose piece. According to the parametric study, mass of the debris was the most important for pressure drop. The lower discharge phenomena could have a significant effect to the total pressure drop of the fuel assembly, approximately 10.8 times for the base case.
© 2021 Korean Nuclear Society, Published by Elsevier Korea LLC. This is an open access article under the CC BY-NC-ND license (http://creativecommons.org/licenses/by-nc-nd/4.0/).

1. Introduction

Flow blockage of the fuel assembly is one of the safety issues in nuclear power plants. In traditional pressurized water reactors (PWRs), it is considered as a decrease of local safety margin due to local flow rate decrease. In terms of the over plant behavior, it is less significant, because there are both intra- and inter-assembly cross flow and blockage area is small compared to flow area of whole core [1]. However, in case of sodium-cooled fast reactors (LMRs), flow blockage of the fuel assembly should be analyzed more carefully. Each fuel assembly is confined with duct to manipulate flow rate through the assembly in most of the LMRs. Therefore, flow blockage of a fuel assembly is directly degraded coolability of the assembly and has potential to progress to core degradation. Due to importance of the flow blockage in the LMRs, even the prototype gen-IV sodium-cooled fast reactor (PGSFR) included flow blockage to the design basis accident [2,3].

Under accident condition, flow blockage usually occurred by molten fuel. Fig. 1 shows general structure of the fuel assembly used in sodium-cooled fast reactor (SFR). Left side of the figure is the top of the assembly. Due to gravity, blockage by molten fuel could occur in the fuel pin region and lower reflector region. If there is no void or vaporization of coolant in the subchannel, ejected fuel solidified just after contact with coolant in the subchannel. In this case, obstacle is generated in the fuel pin region and blocks subchannels. Many literatures analyzed fuel assembly blockage focusing on the blockage at the fuel pin region. Small scale blockage in a single assembly was analyzed by Chang et al. [4]. Temperature was increased more in the fuel and cladding than the coolant. In lead-cooled fast reactor (LFR) ALFRED, blockage at the beginning of the active region was analyzed [5]. The local maximum temperature had linear relationship with blockage ratio, while the maximum temperature at the end of active core showed convex shape until 0.5 of blockage ratio. Raj et al. analyzed porous blockage by both experimental and numerical way [6]. Pressure drop increment by blockage and flow decrement were not significant, however, peak sodium temperature was considerably increased. Nguyen et al. focused on the turbulent characteristics of the flow after blockage by particle-imaged velocimetry (PIV) [7,8]. A pair of counter-rotating vortices were observed in the wake region. Central blockage cases were analyzed by Du et al. [9]. The peak sodium and

* Corresponding author.
** Corresponding author.
E-mail addresses: dwjerng@cau.ac.kr (D.W. Jerng), icbang@unist.ac.kr (I.C. Bang).

https://doi.org/10.1016/j.net.2021.07.012
1738-5733/© 2021 Korean Nuclear Society, Published by Elsevier Korea LLC. This is an open access article under the CC BY-NC-ND license (http://creativecommons.org/licenses/by-nc-nd/4.0/).

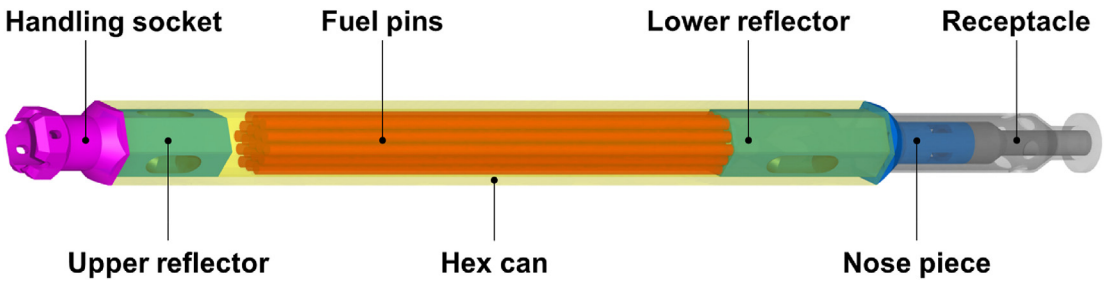

Fig. 1. Schematic of the fuel assembly in SFR.

cladding temperature, and mass flow rate was numerically analyzed with different blockage ratio. Chai et el. analyzed sub-channel blockage in the SFR by numerical way, and there was significant increase of temperature just after the blockage [10]. However, effect of increase pressure drop and corresponding decrease of flow rate was not analyzed.

However, flow blockage at the lower part of the fuel assembly was not analyzed sufficiently. If fuel pin ruptures after sodium boiling, molten fuel flow down downward through the void channel. When the flowing down molten fuel contact to the remaining sodium coolant in the lower structure of the fuel assembly, it is rapidly solidified and blocks the flow channel in the lower structure.

Various papers proposed that sodium boiling could be one of reason for fuel cladding failure [11–14]. Sodium boiling and dryout of coolant degraded cooling of the fuel pin, and the cladding could be failed. Yamano et al. analyzed a hypothetical core disruptive accident (HDCA) in a large scale SFR with SIMMER-III system code [15]. In the unprotected loss of flow (ULOF) accident, sodium boiled before cladding failure. By SAS4A code, which is HCDA analysis code of Argonne national lab., also predicted the sodium boiling before the fuel pin failure under combined LOF and TOP accident in PGSFR [16,17]. Under power excursion, which is same to transient over-power (TOP), pin failed after sodium boiling and relative propagation speed of upward and downward boiling front could be varied depending on the test condition [18]. Jung et al. also reported boiling before pin rupture under ULOF using in-house code [19]. In both CADOR and SPX code, sodium boiled prior to cladding failure under total instantaneous blockage scenario [20].

Regard to lower discharge of the molten fuel and complex phenomena of solidification, blockage, and interaction with lower structures of the fuel assembly were not researched. There were researches related to lower discharge of the molten fuel, however, they only discuss about solidification phenomena in a pool without any structures. It could be represented as jet break-up in a pool. For example, Gabor et el. conducted pool drop experiment with real uranium and sodium, and observed shape and porosity of the debris [21]. Bang et al. employed Wood's metal and water to simulate fuel-coolant interaction [22]. Matsuba et al. simulated lower discharge of molten fuel with sodium and alumina, which focused on the application of the core catcher in the oxide-fueled SFR [23]. Slightly different, Jung et al. observed effect of jet diameter on jet breakup length [24].

However, they did not consider interaction with structure, especially, position of the blockage and porosity. Flow path in the lower structure of the fuel assembly is quite different to the bare pool like jet-breakup experimental condition. Interaction between the structure and descending debris should be considered and also, sedimentation of the debris is important. Those sedimentation of the debris and characteristics of the debris bed like position, porosity, and mass determine pressure drop of the assembly, and finally, coolability of the assembly.

Therefore, in this research, interaction between solidified molten fuel debris and the lower structure of the fuel assembly would be discussed in addition to solidification of the molten fuel. First, LOF-DT experiment was conducted to observe formation of the debris bed in the lower structure. Based on the results of the LOF-DT, pressure drop for intact, and degraded lower structure was experimentally analyzed. Effect of the porosity and mass of the debris bed was parametrically analyzed with CFD.

2. Debris generation experiment - LOF-DT

To evaluate position and location of the debris bed in the lower structure, simulating experiments were conducted. A series of the experiments was named as LOF-DT experiment, which means drop test (DT) under loss of flow condition (LOF). Solidification process of the dropped melt was visualized by high-speed camera, and position of the debris bed was obtained by radiography. Porosity was also measured at each debris bed position.

2.1. Similarity issue

Both molten fuel and sodium requires high level of experimental facility for high temperature and inert atmosphere. Therefore, simulants were used for both melt and coolant. Major properties of original materials and simulants were summarized in Table 1. A prominent characteristic of molten metallic fuel is high density. The other properties like specific heat, thermal conductivity, and surface tension did not show significant difference from other liquid metals. Thus, Wood's metal is the best simulant for metallic fuel. In addition, heat capacity, thermal conductivity, and surface tension of Wood's metal show small discrepancy to the original metal fuel. Wood's metal also has a similarity in terms of crystallization, which would be discussed in the following part. Therefore, Wood's metal was selected as a simulant for the metallic fuel.

Original sodium coolant quenches molten fuel and these quenching and solidification phenomena are our main objective for simulant. So melting point of the fuel simulant should be considered, which is 80 °C for Wood's metal. To simulate quenching of the molten fuel by sodium, a simulant of the sodium should provide sufficient quenching capability. In this point of view, latent heat, thermal conductivity, and boiling point were important. Extraordinary high thermal conductivity of sodium is a characteristic of liquid metal, which could not be observed in non-metallic fluids. Setting aside thermal conductivity, among the candidates, water has the largest latent heat, and proper boiling point for quenching. In addition, water is easy to handle and transparent for visualization. Therefore, water was selected for simulant of the sodium.

Solidification of the molten fuel during quenching could be characterized as crystallization, which is growth of debris. The solidification of the melt and growth of the crystal accompany heat transfer and it could be represented by quenching of the melt by the coolant. It could be expressed like equations below [28]. The

Table 1
Properties of simulants for molten fuel and sodium coolant [25–27].

Material	Melting/Boiling point [°C]	Liquid density [kg/m^3]	Heat capacity [kJ/kg.K]	Thermal conductivity [W/m.K]	Surface tension [N/m]	Latent heat [kJ/kg]
Metal fuel	1077	14,100	0.200	16.0	0.80	88.2
Wood's metal	**80**	**9500**	**0.190**	**13.5**	**~1.0**	**40**
Field's metal	62	6740	0.184	10.0	0.70	25.4
Gallium	29.8	6095	0.365	13.6	0.70	80.2
Molten salt	142	1680	0.156	0.520	0.11	83.7
Sodium	881	1020	1.27	48.9	0.135	3886
Water	**100**	**998**	**4.20**	**0.591**	**0.073**	**2265**
Acetone	56	784	2.14	0.164	0.025	534
Ethanol	78	789	2.46	0.171	0.063	846
Glycerol	290	1261	2.40	0.285	0.063	974

original nomenclature and expression from the textbook were modified for better understanding. It was assumed that heat loss from the melt entirely used in solidification. The relationship between the growth rate of the crystal and heat transfer was summarized in equation (1). Modifying the equation as the expression of growth rate, it could be expressed as equation (2) q is heat flux from the environment to the debris. U, A, and ΔT is overall heat transfer coefficient, area of the debris, and temperature difference between the debris and the environment, respectively. m, t, and h_{fusion} means mass of the debris, time, and latent heat of fusion, respectively.

$$-q = UA\Delta T = \frac{dm}{dt}h_{fusion} \tag{1}$$

$$\frac{dm}{dt} = \frac{UA\Delta T}{h_{fusion}} \tag{2}$$

To consider geometry of the melt in the equation, shape factor α and β were introduced and relationship between the length, area, and mass could be expressed as follows.

$$m = \rho\alpha L^3 \tag{3}$$

$$A = \beta L^2 \tag{4}$$

$$A = \beta\left(\frac{m}{\alpha\rho}\right)^{2/3} \tag{5}$$

Replace the area term in equation (2) by equation (5), equation (6) could be derived. Growth rate of a single debris is proportional to 2/3 power of the mass of the debris at that time, shape factors, heat transfer amount, and heat of fusion. Finally, it could be summarized as equation (7). It was derived from equation (6) using separation of variables. Equation (8) is another form of growth rate in the aspect of length.

$$\frac{dm}{dt} = \beta\left(\frac{m}{\alpha\rho}\right)^{2/3}\frac{U\Delta T}{h_{fusion}} \tag{6}$$

$$\Delta\left(m^{1/3}\right) = \frac{\beta U\Delta T}{3h_{fusion}(\alpha\rho)^{2/3}}t \tag{7}$$

$$\Delta L = \frac{\beta U\Delta T}{3h_{fusion}\alpha\rho} = \frac{\beta q''_{CHF}}{3h_{fusion}\alpha\rho} \tag{8}$$

To calculate growth rate of the debris, heat transfer coefficient and temperature difference should be obtained first. In this study, they were assumed as those at the CHF. Although superheat of the melt in DT experiment was higher than general superheat at CHF, it was still below Leidenfrost temperature. It means that the molten fuel quenched under transition boiling at least. To represent transition and nucleate boiling during complex quenching, CHF was selected as a standard for heat flux for quenching debris. U times ΔT could be simplified as heat flux at the critical heat flux (CHF), like in equation (8). Now, growth rate of the debris in terms of length became a function of CHF, latent heat of fusion, and density of the material.

Length growth rate of the debris in the experiment and actual SFR condition and related parameters are summarized in Table 2. Because similar shape of the debris was expected for the experiment, α and β were assumed as unity for both experiment and actual condition. This assumption was verified by shape of the debris after the experiment. CHF in the experiment was assumed as 1 MW/m^2, which is general CHF value for the water. CHF of sodium was calculated by Caswell and Balzhiser correlation, which is described in equation (9). Based on these, length growth rate in the LOF-DT experiment was calculated as 0.88 mm/s, while 0.89 mm/s was expected in the SFR. The length growth rate in the experiment and in actual SFR condition showed good accordance. Therefore, it could be concluded that similarity of the debris solidification was satisfied in the aspect of growth rate. Test conditions were summarized in Table 3.

$$\frac{q''_{CHF}c_{p,L}\sigma}{h_{fg}^2\rho_V k_L} = 1.18\times10^{-8}\left(\frac{\rho_L-\rho_V}{\rho_V}\right)^{0.71} \tag{9}$$

2.2. Experimental methods

Accident scenario for lower discharge of the molten fuel requires pin rupture after sodium boiling. According to literatures, all kind of accident; ULOF, UTOP, and blockage, could induce lower discharge of the molten fuel. Among the scenarios, ULOF accident had the highest probability [15,16,18]. Moreover, ULOF condition could remove effect of flow and focus on fundamental phenomena. Therefore, zero flow was assumed for our experimental condition.

Due to zero flow condition, the experiment could be simplified as drop test, dropping molten fuel to the experimental apparatus. There were two kinds of test sections. One was roughly similar and transparent for visualization. It is shown on the left side in Fig. 2,

Table 2
Similarity in terms of the growth rate of the debris.

	LOF-DT experiment	SFR
CHF	1.0 MW/m^2	3.3 MW/m^2
Density	9500 kg/m^3	14,100 kg/m^3
Latent heat of fusion	40 kJ/kg	88.2 kJ/kg
Length growth rate	0.88 mm/s	0.89 mm/s

Table 3
Test matrix of LOF-DT series.

#	Melt temperature	Water temperature	Melt mass	Melt velocity	Melt diameter	notes
1	280 °C	10 °C	158 g (13 pin)	1 m/s	1/8″	visualization
2			233 g (19 pin)			repeatability
3						
4						
5	120 °C					lower temp.

and it was approximately 1/2 times scaled down. The other was exact same with the original lower structure of PGSFR. It is shown on the right side in Fig. 2, and exactly 1/2 times scaled down. Therefore, related parameters like diameter, mass of the melt, were selected considering this scale reduction. Fig. 2 shows these two test sections. For the schematic of the transparent section, white regions represent flow path, while sky blue regions represent structures. The transparent section was made of acrylic, plastic, and steel. Inlet and outlet of the lower reflector, nose piece, and orifice has similar shape with the original structures. Three-branched flow path in the middle of the lower reflector was simplified as a single channel. The opaque, exact test section was made by 3-D printer, thus, complex structures like three-branched flow path and multiple orifices were exactly simulated.

For the characteristics of the molten fuel solidification and fragmentation, melt diameter, melt temperature and coolant temperature are important. Because both fuel and cladding are metallic, they generate eutectic, which has approximately 1080 °C of the melting point. Sodium coolant has boiling point approximately 900 °C. It was almost saturated because part of the coolant is already boiled out from the channel according to the accident scenario. Based on this temperature difference, the temperature of the melt was selected as 280 °C, which is 180 °C higher than boiling point of the water. Water temperature was 10 °C to simulate quenching. Mass of the melt was calculated based on the molten volume from Kang and Tentner's work [16,17]. Molten fraction of the fuel was varied from 48% to 53% at cladding failure according to boundary condition. It is equivalent to 10.4–11.5 cm^3 per pin. Considering hexagonal array of the fuel pins, mass of the melt was 233 g in the main experiment, which corresponds to 19 pin failure. Melt velocity was assumed as 1 m/s for running down melt. Diameter of the melt was 1/8″, which is half of the hydraulic diameter of the subchannel in the PGSFR fuel assembly.

DT 01 was focused on the visualization of the phenomena using transparent test section. 02–04 were conducted in the same condition to check repeatability of the experiment. In case of DT 05, melt temperature was decreased to 120 °C to observe effect of superheat.

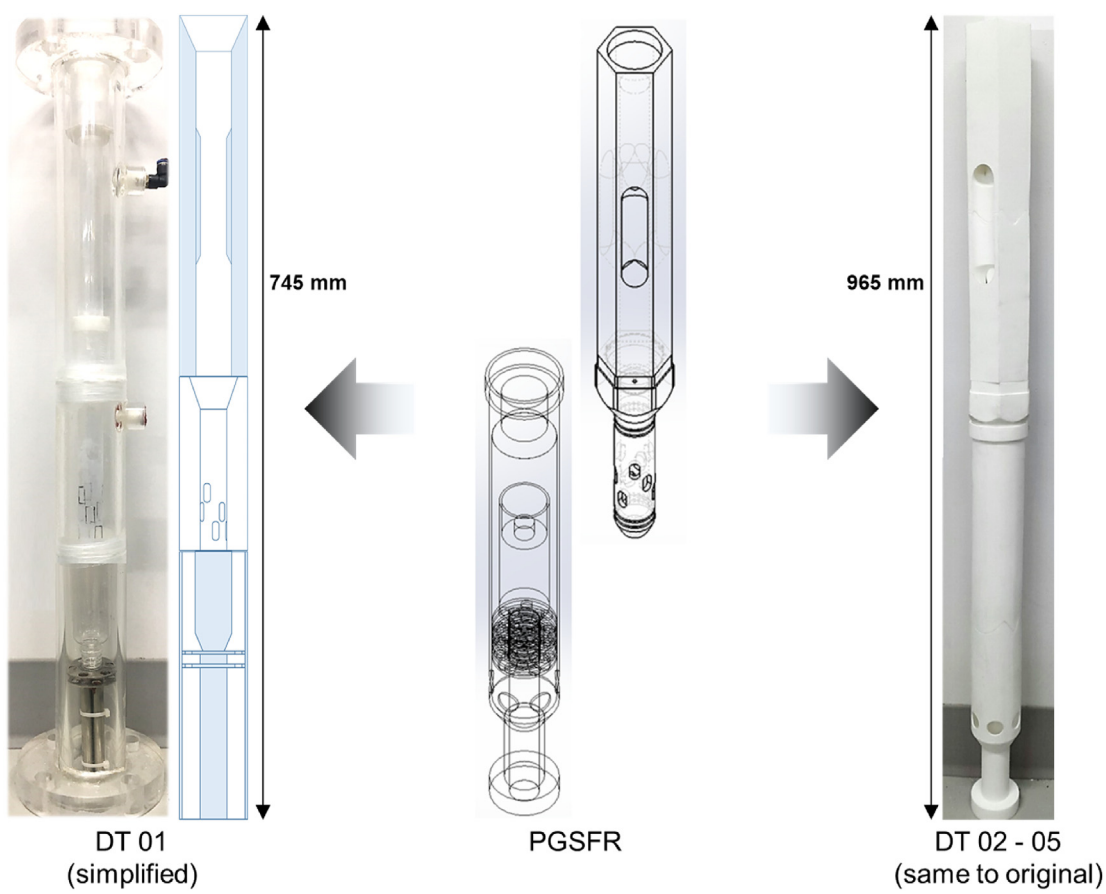

Fig. 2. Test section in LOF-DT series.

2.3. Results and discussion

Overall phenomena were visualized in LOF-DT 01 using transparent test section and high-speed camera. Total 745 mm of the height was visualized as Fig. 3, and the uppermost 200 mm of the test section was magnified to figure out initial stage of the dropping melt. The time interval between each picture was varied to focus on the initial stage. The jet front was emphasized by a yellow arrow at the left side. At the beginning, Wood's metal entered the water and solidified. Solidification could be recognized by the shape of the melt, and reflected light from the surface. At 0.08 s, the melt showed significantly spread shape and the shape of the debris did not changed anymore. Some glittering of the solidified metallic could be also observed. After initial state, due to resistance of the water, speed of falling debris was decreased from the melt velocity and it was converged to the terminal velocity gradually. After the melt was fragmented and sufficiently cooled below the water boiling point, the terminal velocity of the leading edge of the melt at the end of the lower reflector was about 0.55 m/s. After jet front, average velocity of the following debris had lower velocity than the jet front due to eddies, and bubbles by the preceding debris. Approximately 0.3 s, melt reached to the end of the lower reflector, which was the main debris bed region. Small fraction of the debris went further to the nose piece and following debris could not pass through the already generated debris bed.

The result was summarized in Fig. 4. Shape and size of the debris was similar to the that from the experiment with real uranium and sodium. The only difference is sharpness of the debris; debris from the LOF-DT experiment have more blunt edges.

Debris bed was formed by interaction of the fragmented, and solidified melt. As shown in Fig. 4, each debris had some branches from star-shaped body. Therefore, if debris interact, they get tangled each other easily. If size of the agglomerated debris is large enough to get stuck at the bottleneck region, debris bed was formed and following debris are accumulated on the debris. Probability of the interaction among debris could be explained by debris area fraction. Debris area fraction could be expressed by debris area divided by the channel area at a certain cross section of the channel. Equation (10) expresses the relationship among mass flow rate of the debris, density, speed, and summation of the cross-sectional area of the debris at the flow channel. Equation (10) expresses the relationship among mass flow rate, density, speed, and summation of the cross-sectional area of the debris at the flow channel. Here, mass flow rate and density of the debris were constant. In short, decrease of debris falling velocity causes increase of interaction among debris, which forms debris bed at the bottleneck.

There were two bottlenecks in the test section; one was the middle of the lower reflector and the other was lower end of the nose piece. However, there was no debris bed at the middle of the reflector because the melt velocity was fast, and the melt was not solidified yet. In the other region, debris bed was formed because the melt was solidified and slowed down.

Fig. 4 shows the size and shape of the debris and the amount of debris per each debris bed. Shape and size of the debris was similar to the that from the experiment with real uranium and sodium. The only difference is sharpness of the debris; debris from the LOF-DT experiment have more blunt edges. Approximately 116.7 g of the debris were found at the end of the lower reflector, which corresponds to 81.1% of the total melt mass. Once the debris bed is formed, most of the following debris could not go through beyond the debris bed. Because a debris bed acted like a filter, very small debris particle, or debris passed before the debris bed formation could be observed below the debris bed. Some of the debris passed the end of the lower reflector before the debris bed formation, and they were mainly sedimented at the end of the nose piece. Nose piece could be treated with a blocked tube, with several holes on the side like in Fig. 2. Therefore, debris was sedimented on the bottom of the nose piece, and its mass and fraction were 25.1 g, and 17.4%, respectively. Different to debris bed at the end of the lower reflector, debris bed in the nose piece did not have enough height to block the flow path, the several holes. Therefore, some of the debris could escape from the nose piece through the holes. The escaped debris were found in the orifice and the bottom, however, compared to total mass of the melt, they were very small fraction, 1.3 g, and 0.4 g in the orifice and the bottom, respectively. The filtering effect of the debris bed could be recognized by the average debris size. Debris from the lower sedimentation point had small size than debris in the upstream. Mass and porosity of the debris

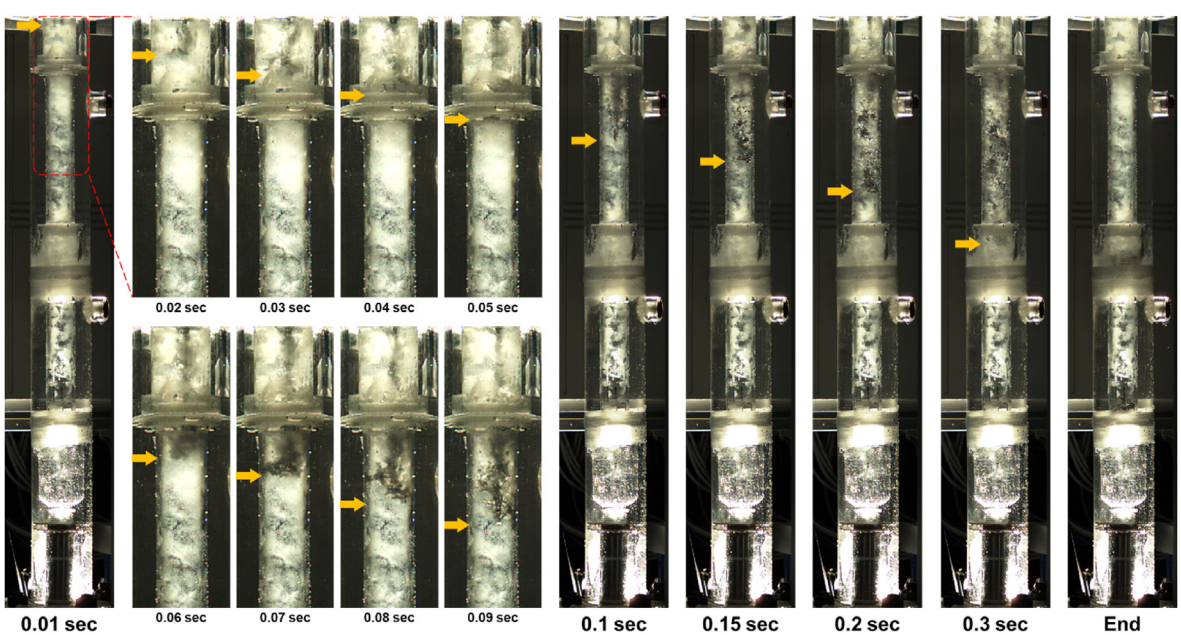

Fig. 3. Breakup and solidification of the melt in LOF-DT 01.

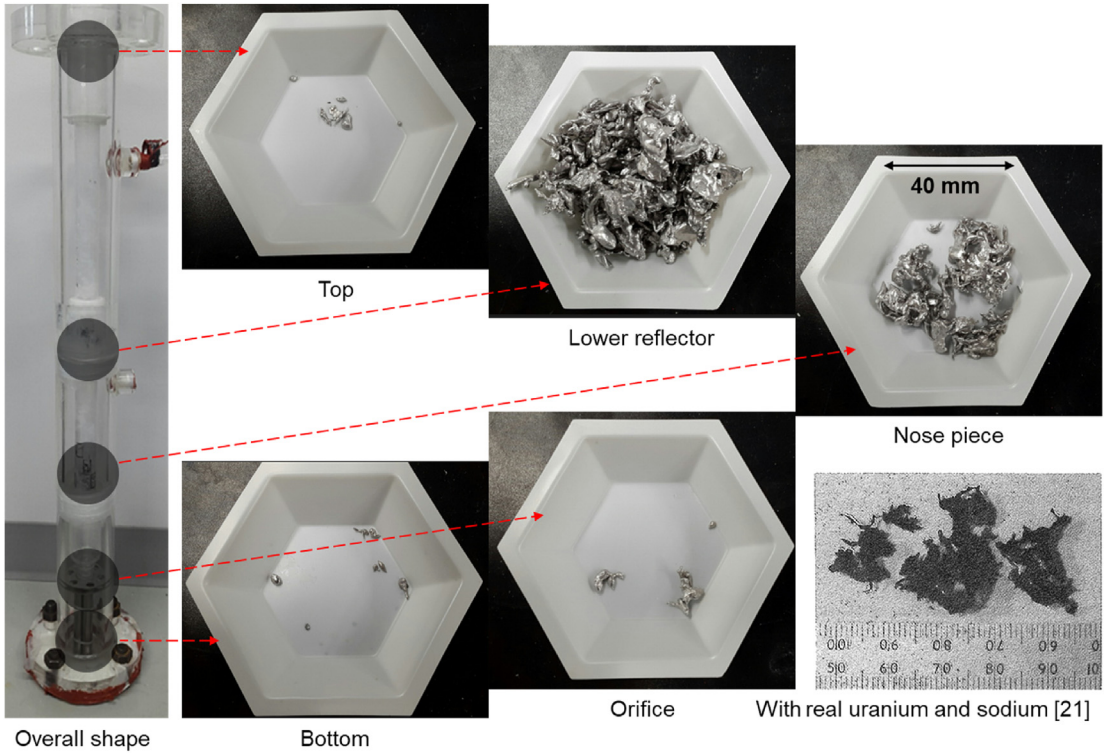

Fig. 4. Debris bed formation in LOF-DT 01.

bed would be discussed with the results from the other experiment in more detail.

$$\dot{m} = \rho u A_{debris} \tag{10}$$

From this visualization analysis, it was found that debris similarity based on crystallization theory is successfully achieved. Even in terms of the porosity, it showed good accordance with the data from the experiment with real sodium and uranium, and it would be discussed in the following section. Area fraction of the debris in the channel cross section was important parameter for debris bed formation. After debris bed formation, most of the debris could not pass through the debris bed and sedimented on the top of the debris bed. Debris in the nose piece, orifice, and the bottom of the test section was the debris that passed before the debris bed formation.

Fig. 5 shows radiography of DT 02 to 05. Because the test section was opaque, to observe debris bed formation inside of the lower structure, it was visualized by non-destructive way as radiography. Thanks to 3-D printing, whole internal structures and complex flow path were fully reflected into the test section. The biggest difference was the three-branched channel in the middle of the lower reflector. In DT 02 to 04, most of the debris were sedimented at the top junction of the three-branched channel. The distance between the top of the lower reflector branch of the three channels was approximately 150 mm. Compared to the result of DT 01, the distance was not enough to decelerate debris to terminal velocity. Area change at the three-branched channel was not also significant; the channel diameter was reduced to 26 mm from 30 mm. Therefore, debris bed formation at the top junction resulted from its geometrical characteristics. Shape of each debris could be recognized in Fig. 4, which seems like a coalescence of pins and spheres. Due to its shape, debris could have agglomerated each other. The length of extended parts of the debris bed into the branch, which seems like tails, slightly changed along experiment. Under same experimental conditions, the length of the tail was varied. As shown in Fig. 6, most of the debris were found at the top junction of the three-branched channel, approximately 80–85% of the total debris. At the nose piece, only 10–15% of the debris were found. There were almost no debris in the receptacle orifice and in the bottom of the facility. Orifice of the receptacle is changed depending on the power of the fuel assembly to make proper flow rate for the assembly, and has only small flow channel through the orifice. Therefore, if debris bed was formed at this region, great increase of the pressure drop was increased. However, there is almost no debris in the receptacle orifice, and it is lucky in terms of safety of the reactor.

Most of the debris were found at the top junction of the three-branched channel, and only small fraction of the debris were in the nose piece. The most noticeable difference in a shape of the debris bed at the top junction. It had shorter tail than debris bed from DT 02–04, while mass of the debris bed was similar. There was probability that the tail of the debris bed dropped to the nose piece during post-processing of the experiment. It caused by characteristics of the debris bed, which is agglomerated by weak interaction between pin like part of each debris. This kind of weak attachment of the tail could be recognized from the other experiment, which could be represented as necking zone in the tail. However, these phenomena were not important in the aspect of debris distribution, porosity of the debris bed and corresponding pressure drop. For DT 05, there was no significant shape difference from the previous cases. Therefore, effect of melt temperature on the coolability of the fuel assembly is negligible, while only shape of the debris bed was slightly changed.

Debris distribution in LOF-DT experiments were summarized in Fig. 6. Most of the debris were sedimented in the lower reflector, and others were in the nose piece. Mass fraction of the debris were approximately 80–90% and 10–20%, at the lower reflector and nose

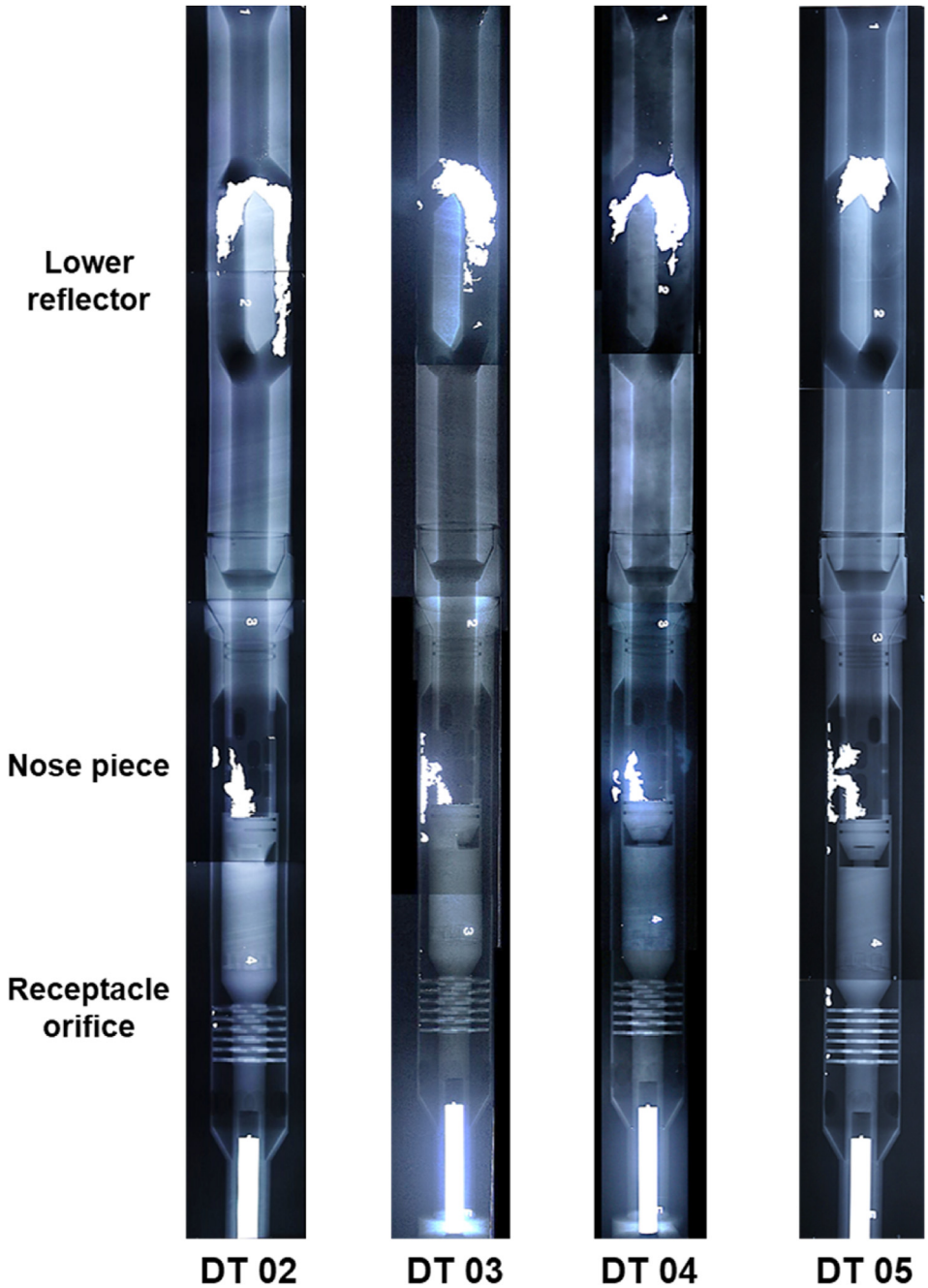

Fig. 5. Debris bed formation in DT 02–05.

piece, respectively. This tendency was not changed in DT 05, therefore, the fact that effect of melt temperature could be negligible could be checked once again. Only negligible amount of the debris was found on the receptacle orifice; less than 5%.

In the accident situation, decay heat was removed by the natural circulation. To evaluate degradation of the natural circulation by lower discharge of the molten fuel, porosity of the debris bed should be obtained in addition to the debris bed position. Porosity was observed at each sedimentation point, the lower reflector and nose piece. Porosity was obtained by two method to recognize closed pore and reduce error. One was volume-based method, which measure volume of the debris directly using measuring cylinder. The other one was mass-based methods, which measures mass of the debris. If volume-based porosity is significantly larger than mass-based porosity in most of the experiment, it means that there are closed pores. The results were summarized in Table 4. For both locations, the volume-based porosity and the mass based-porosity showed similar values. Therefore, there was no meaningful difference of volume-based and mass-based porosity, and there was no closed pore.

2.4. Summary of LOF-DT experiment

By LOF-DT experiment, location, mass fraction, and porosity of the debris bed were obtained. Main sedimentation points were the lower reflector, where approximately 85% of the debris were found, and the nose piece, where approximately 15% of the debris were found. Porosity was 0.7 in the lower reflector, and 0.85 in the nose

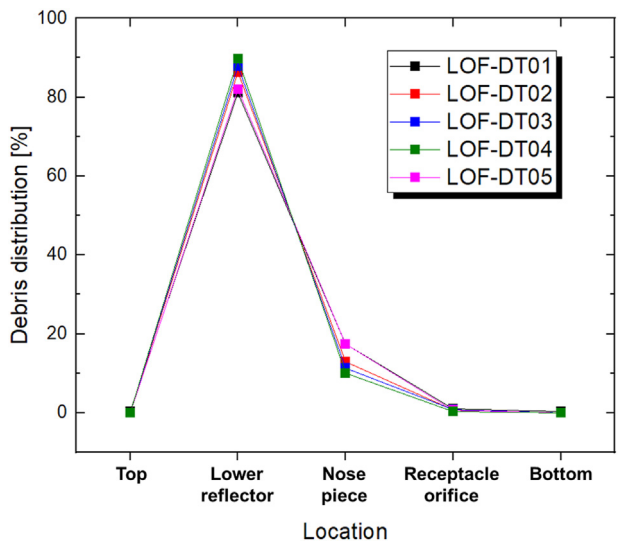

Fig. 6. Summary of debris mass distribution.

Table 4
Porosity of the debris bed.

Location	Experiments	Porosity	
		(vol. based)	(mass based)
Lower reflector	1	83.3%	84.6%
	2	73.2%	70.1%
	3	70.5%	67.8%
	4	70.2%	69.8%
	5	65.4%	66.3%
	Average	**72.5%**	**71.7%**
Nose piece	1	79.6%	84.5%
	2	86.5%	83.8%
	3	88.1%	86.8%
	4	84.7%	87.8%
	5	82.9%	84.3%
	Average	**84.4%**	**85.4%**

piece, approximately. There was no closed pore in the debris bed. The debris beds were not found in the orifice, where small amount of debris could induce large pressure drop.

3. Pressure drop analysis

Increase of the pressure drop of the fuel assembly degrades its coolability. In this section, pressure drop experiment was designed based on the result from the LOF-DT experiment, considering characteristics of the debris bed. Pressure drop increment by the debris bed would be experimentally studied. Based on the pressure drop experiment, it was also parametrically studied using CFD.

3.1. Similarity issue

For better similarity, test sections were made in the realistic scale, and only working fluid was changed to the water. Regard to calculation of the similarity parameter, velocity at the united flow path of the lower reflector was selected as a representative velocity. Flow rate during natural circulation was assumed as 3% of the total flow rate, which corresponds to 0.306 m/s in the representative position. It was equivalent to Reynolds number as 6.692 x 10^4. To make same Reynolds number with water, 1.46 m/s of the velocity was required. Related parameters were summarized in Table 5. These values were applied to the CFD analysis in common.

Table 5
Summary of similarity for pressure drop experiment.

	PGSFR	Experiment
Working fluid	Sodium	Water
Density [kg/m^3]	828	999
Velocity [m/s]	0.306	1.46
Diameter (representative) [m]	0.06	
Viscosity	0.227 x 10^{-3}	1.310 x 10^{-3}
Reynolds number	6.692 x 10^4	
Note	@ 800 K	@ 10 °C

Table 6
Summary of uncertainty analysis.

Category	Contributor	Magnitude
Pressure gauge	Transmitter	0.25%
	Void	0%
	Isolator	0.1%
	Input/Output	0.01%
	ADC conversion	0.003%
	Total	**2.7% (8.08 kPa)**
Differential pressure gauge	Transmitter	0.1%
	Void	0%
	Isolator	0.1%
	Input/Output	0.01%
	ADC conversion	0.003%
	Total	**0.14% (0.035 kPa)**
Flow meter	Transmitter	0.5%
	Isolator	0.1%
	Input/Output	0.01%
	ADC conversion	0.003%
	Total	**0.5%**

3.2. Pressure drop experiment

3.2.1. Experimental method

The test sections were made by 3-D printer, and summarized in Fig. 7. Grey part, blue part, and red part represent the structure, flow path, and debris bed, respectively. There were a pair of test sections for each part; one was original structure without debris bed and the other one was a test section with debris bed. Nose piece was made with covering part of the receptacle to simulate realistic flow channel. For the lower reflector, there is a hex can outside and it covers three-branched flow path of the lower reflector. It was simulated as covering part outside of the channel. The debris bed was modeled as a porous body. Considering porosity of the debris from the LOF-DT test in a conservative manner, porosity of the lower reflector was selected as 0.6, while that of the nose piece was 0.8. Information of porous geometry was also summarized in Fig. 7.

Test loop for the pressure drop test were summarized in Fig. 8. Centrifugal pump and electromagnetic flow meter were employed. Pressure was measured by both a differential pressure gauge and pressure tap to cover various pressure range.

Uncertainties were also analyzed in the pressure drop test. Total error was calculated using error propagation method. Error of the transmitter were 0.25%, 0.1%, and 0.5% for the pressure gauge, differential pressure gauge, and flow meter, respectively. The isolator, input/output, and ADC conversion were commonly employed. Finally, error for the pressure gauge, differential pressure gauge, and the flow meter was 8.08 kPa, 0.035 kPa, and 0.5%, respectively. The error range for all parameters was small enough to secure high resolution for the results. Uncertainty of each parameter and its contributors were sumarized in Table 6.

3.2.2. Experimental results

Experimental results were taken as an average of 10 times of repeated experiment, and there was no outlier. Average pressure drop and standard deviations were summarized in Table 7. Regard

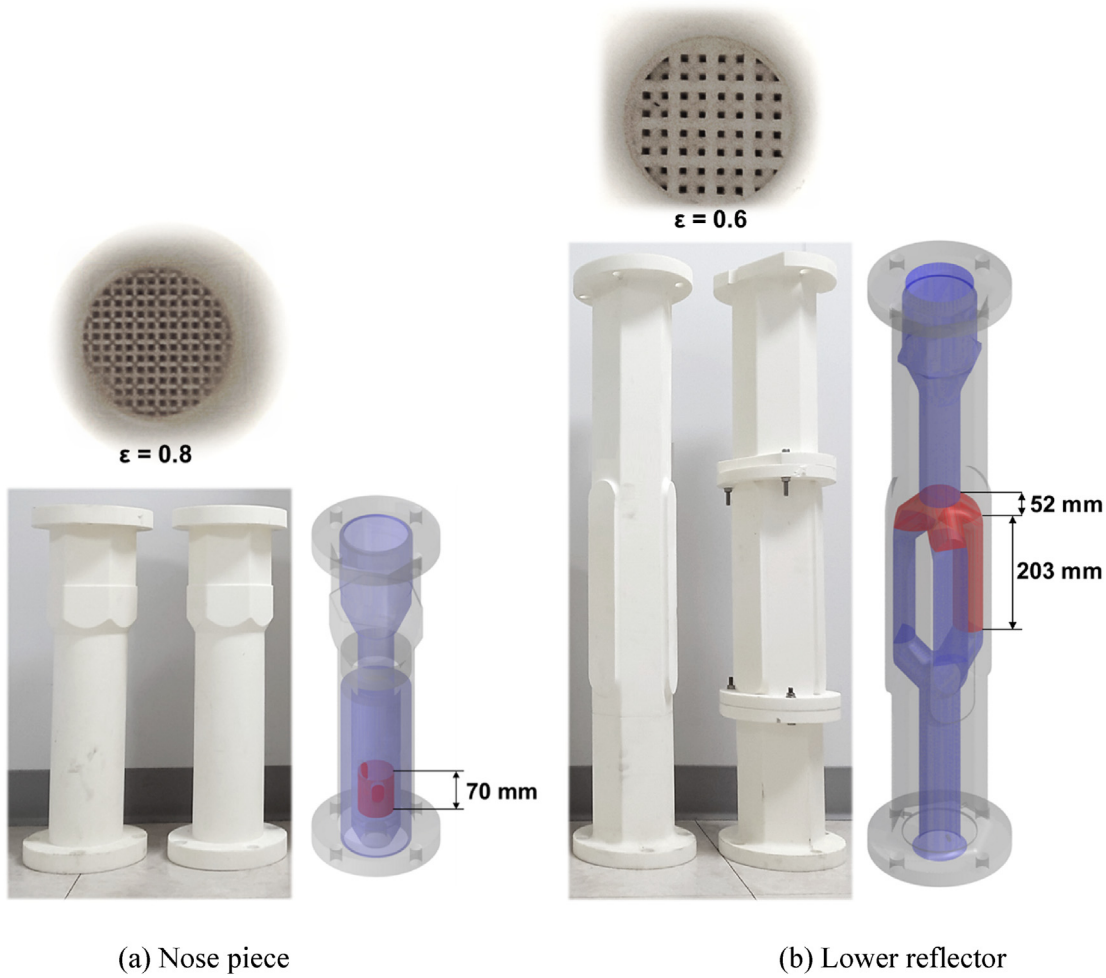

Fig. 7. Test section of the pressure drop experiment.

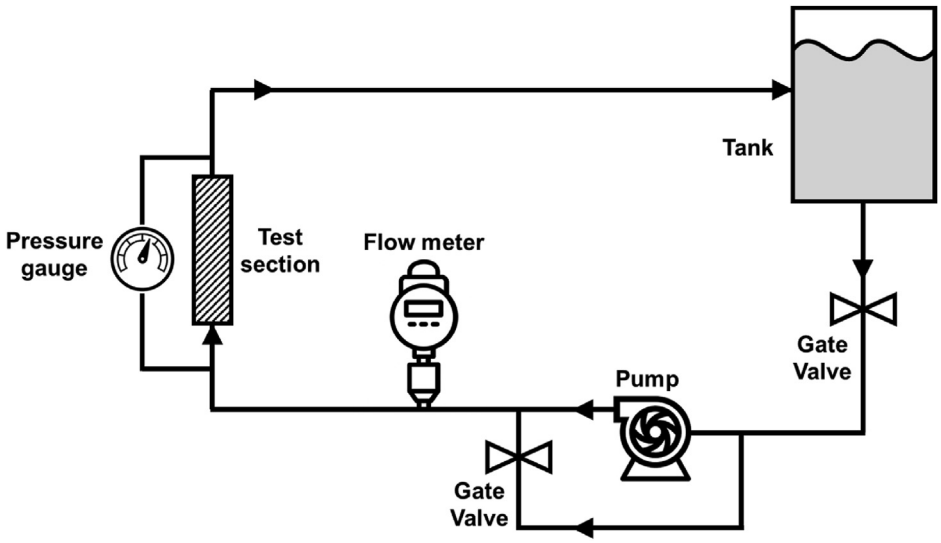

Fig. 8. Schematic of the pressure drop test loop.

to lower reflector, 1.34 kPa of the pressure drop was obtained for the bare case, while 160.51 kPa was obtained for the case with debris. Compared to the bare case, pressure drop was drastically increased approximately 120 times. As shown in Fig. 7, blockage by debris bed was in the upper junction, and one of the three-branched channel. There was no bypass between the inlet and

Table 7
Results of pressure drop experiment.

Part		Porosity	Pressure drop	Error (Reading to error)
Lower reflector	Bare	–	1.34 kPa ±0.02 kPa	0.035 kPa (2.6%)
	With debris	0.6	160.51 kPa ±2.88 kPa	8.08 kPa (5.0%)
Nose piece	Bare	–	1.67 kPa ±0.02 kPa	0.035 kPa (2.1%)
	With debris	0.8	1.86 kPa ±0.02 kPa	0.035 kPa (1.9%)

outlet of the test section, in other words, flow should pass through the porous region, which causes great increase of the pressure drop. Regard to the nose piece, 1.67 kPa of the pressure drop was measured for the bare case, while 1.86 kPa of the pressure drop was measured for the case with debris. Different to the lower reflector case, there was no great increase of the pressure drop. Only 0.19 kPa of the pressure drop increased by the debris bed. However, it was still clear increase because resolution of the experiment was 0.035 kPa. There was no great increase of the pressure drop for the nose piece. First, porosity of the debris bed in the nose piece was 0.8, while that in the lower reflector was 0.6. More important reason was existence of the bypass. As shown in Fig. 7, there were many bypasses of the debris bed. There were nine holes on the bottom part of the side, which were arranged in 3 by 3 with slightly dislocated in vertical. The representative debris bed in the experiment only affected to three holes in the lowest raw of the arrangement. There were still six holes which were free from the effect of the porous body. Therefore, there was no great increase of the pressure drop in the nose piece.

3.3. Parametric study using CFD

3.3.1. Modeling in CFD

Effect of porosity and debris melt were analyzed by CFD. To have accordance with experiments, base cases were fitted to the experimental results. Number of mesh was 0.38 and 0.33 million for the lower reflector and nose piece, respectively. Porosity was given as 0.6 and 0.8 for the lower reflector and nose piece, which were the same to the experimental result. To make same pressure drop with experiment for base case, permeability for porous body was 4.74 x 10^{-10}, and for 1.00 x 10^{-10} the lower reflector and nose piece, respectively. Considering wall-dominant characteristic of the current geometries, SST model was adopted for the turbulent model, and heat transfer model was excluded because it was pressure drop analysis.

3.3.2. Result of parametric study

Effect of the mass, and porosity of the debris bed was parametrically studied by CFD. First, CFD results were fitted to the experimental results by manipulating permeability of the porous body. For the lower reflector, pressure drop by the CFD was 160.27 kPa, while 160.51 kPa was the experimental results. Regard to nose piece, 1.91 kPa of the pressure drop obtained by the CFD while 1.86 kPa was the experimental results. CFD showed good accordance with experimental results.

If mass of the debris bed changes, its volume also changes. In case of the lower reflector, it was treated as number of blocked channels in the lower reflector. Base case was fitted to the experiment, which was one of the three-branched channel blockage. In the parametric study, number of blocked channels was increased to two and three. In case of porosity, it was increased and decreased by 0.1, from 0.6 of the original porosity. For the nose piece, mass of the debris was reflected as height change of the debris bed. Porosity was also increased and decreased by 0.1 from 0.8 of the original porosity.

In Table 8, Figs. 9 and 10, results of the parametric study on the lower reflector and nose piece were summarized. In case of 0.7 of the porosity, pressure drop decreased to 137.67 kPa, which was 14.1% decreased from the original pressure drop. If debris bed became denser, in case of 0.5 of porosity, 192.06 kPa of the pressure drop was observed. Here, increment and decrement of the porosity was the same, however, change of the pressure drop was more sensitive for decreasing of porosity. Regard to the additional blockage, 229.71 kPa of the pressure drop was observed for one additional blockage case. However, in case of all three channels blockage, pressure drop was greatly increased to 851.50 kPa, more than five times of the base case. A channel for bypass of the flow was the most important factor for increase of the pressure drop. As shown in Fig. 9, in case of 1 and 2 channel blocked, flow was concentrated to the channel without blockage, which was called a bypass. However, if all channels were blocked, flow became evenly distributed and had large pressure drop during passing through the porous blockage.

Regarding the nose piece, the most interest thing was that pressure drop did not change as porosity was changed. Regardless to the porosity, most of the flow was flow into the other unblocked holes, therefore, pressure drop was not significantly changed. Because the debris bed only blocks three of the nine holes, flow was concentrated to the other unblocked six holes and pressure drop did not change, as 1.91 kPa. However, the pressure drop was considerably changed depending on the height of the sedimentation, which is related to the blockage of the holes. If the sedimentation height became half of the original, which blocks approximately 1/4 of the three holes in the bottom raw, the pressure drop was decreased to 1.57 kPa. In case of doubled sedimentation height, pressure drop was greatly increased to 14.50 kPa, which was more than 6.5 times of the increase compared to the base case. It could be by explained by the change of the unblocked holes. If debris bed accumulated to 140 mm from the bottom of the nose piece, it was enough to cover six holes in the bottom and middle raw. Additionally, it also covered approximately 2/3 of the three holes in the top raw. In terms of the bypass, bypass was decreased to 1/6, compared to the original six holes. Therefore, there was a great increase of pressure drop in the case of increased sedimentation height. From the results of the parametric study, the

Table 8
Summary of the parametric study.

Component	Condition		Pressure drop	Change rate
	Porosity	Debris bed		
Lower reflector	0.5	1 channel blocked	192.06 kPa	+19.5%
	0.7		137.67 kPa	- 14.1%
	0.6		**160.27 kPa**	–
		2 channel blocked	229.71 kPa	+42.1%
		3 channel blocked	851.50 kPa	+531.3%
Nose piece	0.7	70 mm sedimented	1.91 kPa	+0.0%
	0.9		1.91 kPa	+0.0%
	0.8		**1.91 kPa**	–
		35 mm sedimented	1.57 kPa	−17.8%
		140 mm sedimented	14.50 kPa	+659.2%

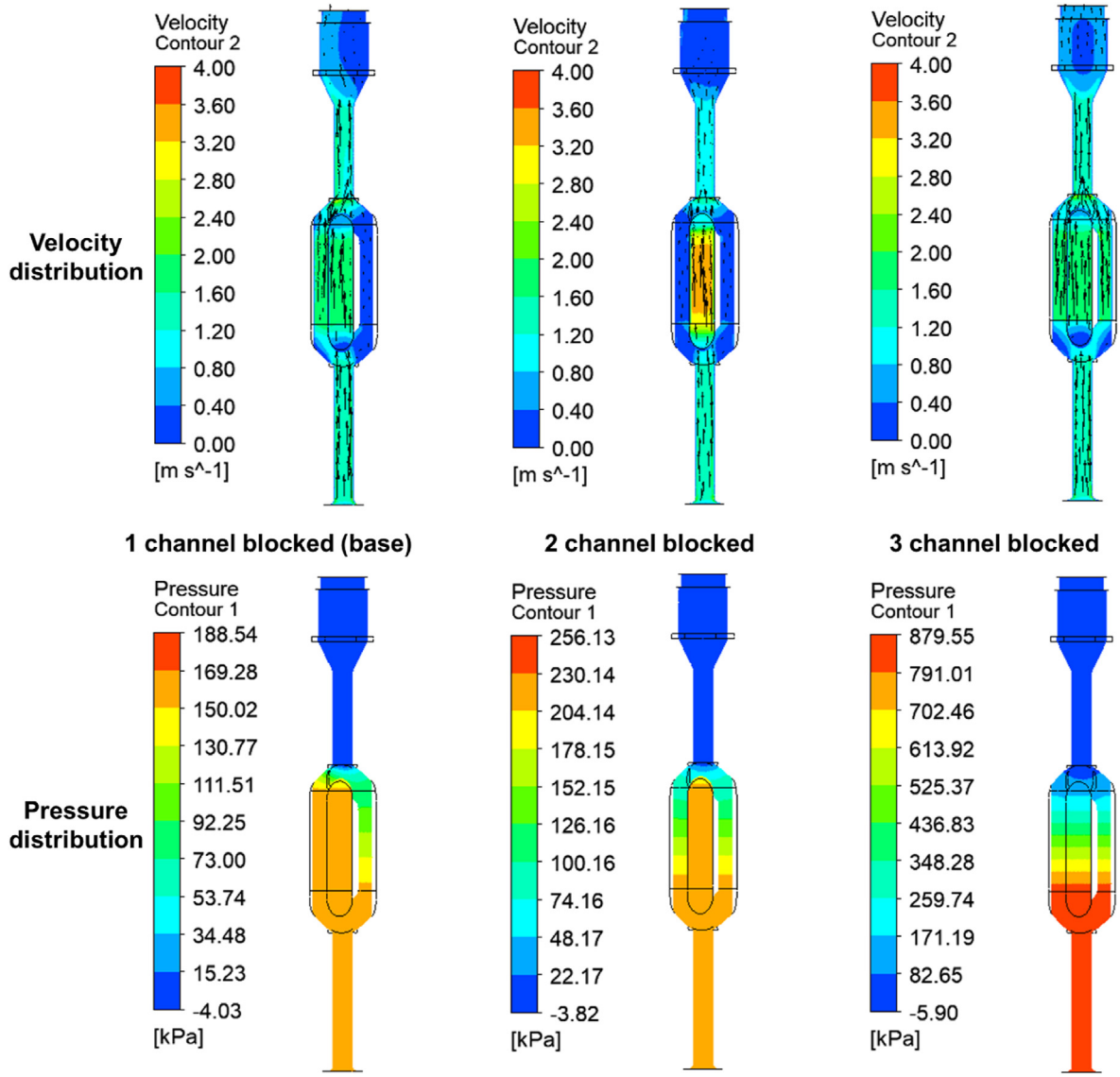

Fig. 9. Pressure and velocity distribution in the lower reflector.

most important thing was the bypass for the pressure drop. To make bypass, distribution of the randomly dropped debris to the three channels was important in the lower reflector, and the mass of the debris was important in the nose piece.

3.4. Summary of the pressure drop analysis

In terms of the pressure drop of the whole fuel assembly, the lower reflector and nose piece only occupy 8.2% and 1.9% of the total pressure drop of the fuel assembly. Although they contributed only 10% of the pressure drop, increase rate of the pressure drop was significant. After downward discharge of the molten fuel, increment of the total pressure drop of the fuel assembly could be significant. For the base case, pressure drop of the lower reflector was increased 120 times, while that of the nose piece was increased 10%, approximately. Applying increased pressure drop for corresponding part of the fuel assembly, total pressure drop of the assembly was increased to 10.8 time of the intact fuel assembly. It was significant amount of the increase. If characteristics of the debris changes, it could be increase more. Therefore, lower discharge of the molten fuel could cause significant degradation of the coolability of the fuel assembly.

4. Conclusion

From the LOF-DT experiment, which was designed to obtain the characteristics of the debris bed, the position and porosity of the debris bed were obtained. Most of the debris were sedimented in the lower reflector, and the others were in the nose piece approximately 85% and 15%, respectively. Porosity of the debris bed was higher in the nose piece. In the lower reflector, 0.7 of the porosity was observed, while 0.85 of the porosity was observed in the nose piece.

This debris bed made pressure drop of corresponding part increase significantly, especially in the lower reflector. It was increased from 1.34 kPa to 160.51 kPa after debris sedimentation. However, only 10% of the pressure drop increased in the nose piece. Regard to lower reflector, if porosity of the debris bed was decreased 0.1, the pressure drop was increased 19.5%, while increasing 0.1 of the pressure drop made 14.1% of the pressure drop

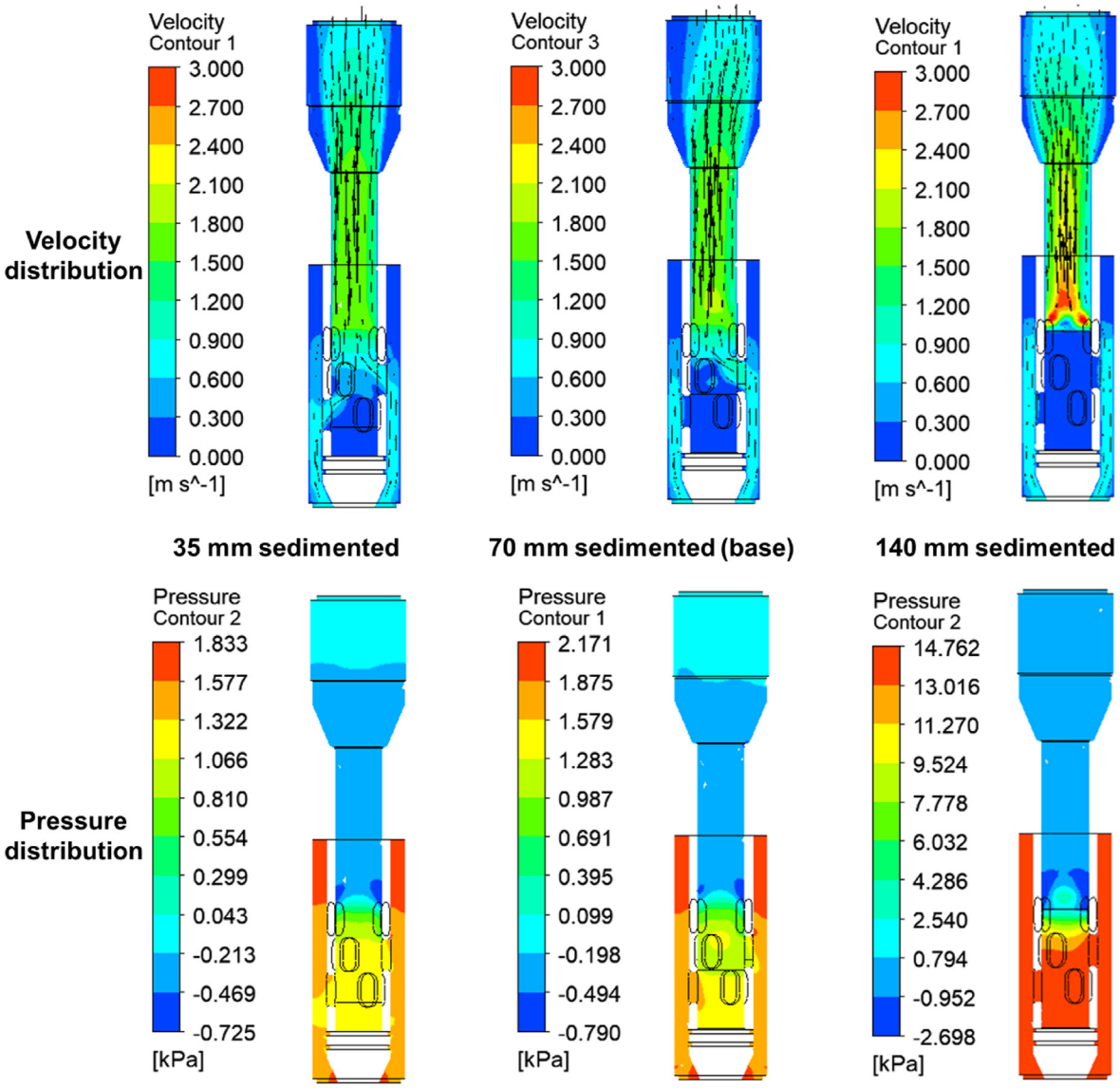

Fig. 10. Pressure and velocity distribution in the nose piece.

decrease. The important factor for the pressure drop is the number of the blocked channel, which was related to the mass of the debris. Compared to the 1 channel blocked case, 42.1% and 531.3% of the pressure drop increased for 2 and 3 channel blocked case in the lower reflector. Similar tendency was observed for the nose piece. There was no significant change of the pressure drop depending on change of the porosity. However, pressure drop increased more than 6 times for doubled debris bed mass. Although there was no significant blockage by low-porosity debris at the weak points like holes of the orifice or small inlets, the lower discharge phenomena could have a significant effect to the total pressure drop. For the base case, 10.8 time of the pressure drop increased in the aspect of the fuel assembly.

Coolability of the damaged assembly should be discussed with more comprehensive analysis with flow distribution among the intact and damaged assemblies. Because the LOF was assumed, cooling of the assembly depends on the natural circulation. Further research on the flow distribution among the assemblies and degradation of the coolability by the pressure drop increased is required.

Declaration of competing interest

We certify that there is no conflict of interest including any financial, personal or other relationships with other people or organizations within three years of beginning the submitted work that could inappropriately influence, or be perceived to influence, our work.

Acknowledgement

This work was supported by the Nuclear Energy Research Program through the National Research Foundation of Korea (NRF) funded by the Korea government(MSIT) (No. 2017M2A8A6015826, 2020M2A8A4022882, 2017M2A8A2018595).

References

[1] C. Alison, E. Balabanov, F. D'Auria, J. Misak, C. Munhoz-Camargo, S. Salvatores, V. Snell, Accident Analysis for Nuclear Power Plants with Pressurized Water Reactors, IAEA, 2003.
[2] K.L. Lee, K.S. Ha, J.H. Jeong, C.W. Choi, T. Jeong, S.J. Ahn, S.W. Lee, W.P. Chang,

S.H. Kang, J. Yoo, A preliminary safety analysis for the prototype gen IV sodium-cooled fast reactor, Nuclear Engineering and Technology 48 (2016), 1171-1082.
[3] H. Shin, M. Jae, An accident sequence analysis for PGSFR, in: Proceedings of Korean Nuclear Society Autumn Meeting, Gyeongju, Korea, October 26-27, 2017.
[4] W.P. Chang, K.L. Lee, S.H. Kang, C.W. Choi, H.Y. Jeong, Investigation of axial blockage position effect in the SFR flow blockage analysis, in: Proceedings of Korean Nuclear Society Autumn Meeting, Gyeongju, Korea, October 25-26, 2012.
[5] I.D. Piazza, F. Magugliani, M. Tarantino, A. Alemberti, A CFD analysis of flow blockage phenomena in ALFRED LFR demo fuel assembly, Nucl. Eng. Des. 276 (2014) 202–215.
[6] M.N. Raj, K. Velusamy, R.K. Maity, Thermal hydraulic investigations on porous blockage in a prototype sodium cooled fast reactor fuel pin bundle, Nucl. Eng. Des. 303 (2016) 88–108.
[7] T. Nguyen, L. White, R. Vaghetto, Y. Hassam, Turbulent flow and vortex characteristics in a blocked subchannel of a helically wrapped rod bundle, Exp. Fluid 60 (2019) 129–156.
[8] T. Nguyen, R. Vaghetto, Y. Hassam, Experimental investigation of turbulent wake flows in a helically wrapped rod bundle in presence of localized blockages, Phys. Fluids 32 (2020), 075113.
[9] P. Du, J. Shan, Bo Zhang, L.K.H. Leung, Thermal-hydraulics analysis of flow blockage events for fuel assembly in a sodium-cooled fast reactor, Int. J. Heat Mass Tran. 138 (2019) 496–507.
[10] X. Chai, L. Zhao, W. Hu, Y. Yang, X. Liu, J. Xiong, X. Cheng, Numerical investigation of flow blockage accident in SFR fuel assembly, Nucl. Eng. Des. 359 (2020), 110437.
[11] Y. Kikuchi, K. Haga, Sodium boiling experiments in a 19-pin bundle under loss-of-flow condition, Nucl. Eng. Des. 66 (1981) 357–366.
[12] K. Yamaguchi, Flow patterns and dryout under sodium boiling conditions at decay power levels, Nucl. Eng. Des. 99 (1987) 247–263.
[13] H. Ninokata, Analysis of low-heat-flux sodium boiling test in a 37-pin bundle by the two-fluid model computer code SABENA, Nucl. Eng. Des. 97 (1986) 233–246.
[14] N. Alpy, P. Marsault, M. Anderhuber, A. Gerschenfeld, P. Sciora, D. Kadri, J. Perez, R. Lavastre, Phenomenological investigation of sodium boiling in a SFR core during a postulated ULOF transient with CATHARE 2 system code: a stabilized boiling case, J. Nucl. Sci. Technol. 53 (2016) 692–697.
[15] H. Yamano, Y. Tobita, S. Kubo, N. Ueda, Event sequence analysis of core disruptive accident in a metal-fueled sodium-cooled fast reactor, in: Proceedings of NTHAS10: the Tenth Korea-Japan Symposium on Nuclear Thermal Hydraulics and Safety Kyoto, Japan, November 27-30, 2016.
[16] S.H. Kang, A. Tentner, A. Karahan, K.L. Lee, LOF and TOP severe accident analysis for PGSFR using SAS4A metal fuel version code, in: Proceedings of Korean Nuclear Society Autumn Meeting, Gyeongju, Korea, October 26-27, 2017.
[17] A.M. Tentner, A. Karahan, S.H. Kang, Overview of the SAS4A metallic fuel models and extended analysis of a postulated severe accident in the prototype gen-IV sodium-cooled fast reactor, Nucl. Technol. 206 (2020) 242–254.
[18] K. Herbreteau, N. Marie, F. Bertrand, J.-M. Seiler, P. Rubiolo, Sodium-cooled fast reactor pin model for predicting pin failure during a power excursion, Nucl. Eng. Des. 335 (2018) 279–290.
[19] H.W. Jung, H.K. Song, Y.J. Kim, S.B. Moon, H. Heo, I.C. Bang, Y.B. Jo, H.Y. Choi, S.H. Park, T.H. Lee, E.S. Kim, S.H. Kang, D.W. Jerng, Effect of burnup on molten fuel behavior under hypothetical core disruptive accident (HCDA) condition in PGSFR, in: Proceedings of Korean Nuclear Society Autumn Meeting Yeosu, Korea, October 25-26, 2018.
[20] T. Rahm, J.-B. Droin, N. Marie, F. Bertrand, A. Marrel, Analysis of the Total Instantaneous Blockage accident consequences in the innovative inherently-safe CADOR SFR core, Nucl. Eng. Des. 348 (2019) 78–89.
[21] J.D. Gabor, R.T. Purviance, R.W. Aeschlimann, B.W. Spencer, Characterization of IFR metal fuel fragmentation, in: Proceedings of Annual Meeting of the American Nuclear Society, Dallas, TX (USA), Jun 7-11, 1987.
[22] K.H. Bang, J.M. Kim, D.H. Kim, Experimental study of melt jet breakup in water, J. Nucl. Sci. Technol. 40 (2003) 807–813.
[23] K. Matsuba, M. Isozaki, K. Kamiyama, Y. Tobita, Distance for fragmentation of a simulated molten core material discharged into a sodium pool, J. Nucl. Sci. Technol. 53 (2016) 707–712.
[24] W.H. Jung, H.S. Park, K. Moriyama, M.H. Kim, Analysis of experimental uncertainties in jet breakup length and jet diameter during molten fuel-coolant interaction, Nucl. Eng. Des. 344 (2019) 183–194.
[25] M.H. Lee, H. Heo, D.W. Jerng, I.C. Bang, Phenomenological study on the Ex-pin phenomena in the initial phase of HCDA on metal-fueled SFR using simulant, Ann. Nucl. Energy 130 (2019) 34–46.
[26] J.K. Fink, L. Leibowitz, Thermodynamic and Transport Properties of Sodium Liquid and Vapor, No. ANL–RE-95/2, Argonne National Lab., 1995.
[27] A.K. Raj, R. Subramanian, R.N. Hajra, H. Tripathy, M. Rengachari, S. Saibaba, Calorimetric study of phase stability and phase transformation in U-xZr (x = 2, 5, 10 wt pct) alloys, Metall. Mater. Trans. 46 (2015) 4986–5001.
[28] J.W. Mullin, Crystallization, Elsevier, 2001.